In vivo molecular imaging of breast cancer metabolic heterogeneity using [1-^{13}C]pyruvate-d$_3$ hyperpolarized by reversible exchange with parahydrogen

*Stefan Petersen,‡ Luca Nagel,‡ Philipp R. Groß, Henri de Maissin, Robert Willing, Lisa Heß, Julia Mitschke, Nicole Klemm, Judith Treiber, Christoph A. Müller, Stephan Knecht, Ilai Schwartz, Moritz Weigt, Michael Bock, Dominik von Elverfeldt, Maxim Zaitsev, Eduard Y. Chekmenev, Jan-Bernd Hövener, André F. Martins, Franz Schilling, Thomas Reinheckel, Andreas B. Schmidt**

‡ shared first authorship

* correspondence: andreas.schmidt@uniklinik-freiburg.de

S. Petersen, P. R. Groß, H. de Maissin, R. Willing, C. A. Müller, M. Weigt, M. Bock, D. von Elverfeldt, M. Zaitsev, A. B. Schmidt
Division of Medical Physics, Department of Radiology, University Medical Center Freiburg, Faculty of Medicine, University of Freiburg, Killianstr. 5a, Freiburg 79106, Germany

P. R. Groß, H. de Maissin, R. Willing, L. Heß, M. Bock, D. von Elverfeldt, M. Zaitsev, T. Reinheckel, A. B. Schmidt
German Cancer Consortium (DKTK), partner site Freiburg and German Cancer Research Center (DKFZ), Im Neuenheimer Feld 280, Heidelberg 69120, Germany

L. Nagel, F. Schilling
Department of Nuclear Medicine, TUM School of Medicine and Health, TUM University Hospital, Technical University of Munich, Munich, Germany, Ismaninger Str. 22, Munich 81675, Germany

L. Heß, J. Mitschke, J. Treiber, N. Klemm, T. Reinheckel
Institute of Molecular Medicine and Cell Research, Faculty of Medicine, University of Freiburg, Stefan-Meier-Str. 17, Freiburg 79104, Germany

C. A. Müller, S. Knecht, I. Schwartz
NVision Imaging Technologies GmbH, Wolfgang-Paul-Str. 2, Ulm 89081, Germany

E. Y. Chekmenev, A. B. Schmidt
Department of Chemistry, Integrative Biosciences (Ibio), Karmanos Cancer Institute (KCI), Wayne State University, Detroit, Michigan 48202, United States

J.-B. Hövener
Section Biomedical Imaging, Molecular Imaging North Competence Center MOINCC, Department of Radiology and Neuroradiology, University Hospital Schleswig Holstein, Kiel University

A. F. Martins
Werner Siemens Imaging Center, Department of Preclinical Imaging and Radiopharmacy, Eberhard Karls University Tübingen, Röntgenweg 13, Tübingen 72076, Germany

A. F. Martins
Cluster of Excellence iFIT (EXC 2180) "Image-Guided and Functionally Instructed Tumor Therapies", Eberhard Karls University Tübingen

A. F. Martins
German Cancer Consortium (DKTK), partner site Tubingen and German Cancer Research Center (DKFZ), Im Neuenheimer Feld 280, Heidelberg 69120, Germany

T. Reinheckel
Centre for Biological Signalling Studies BIOSS, University of Freiburg, Freiburg 79104, Germany

F. Schilling
Munich Institute of Biomedical Engineering, Technical University of Munich, Garching, Germany, Boltzmannstr. 11, Garching 85748, Germany

F. Schilling
German Cancer Consortium (DKTK), partner site Munich and German Cancer Research Center (DKFZ), Im Neuenheimer Feld 280, Heidelberg 69120, Germany

Abstract

Metabolic MRI using hyperpolarized (HP) [1-^{13}C]pyruvate is promising for diagnostic medicine, allowing the study of cancer metabolism and early detection of therapy response. However, a possible widespread and routine use requires high-throughput and user-friendly technologies to produce the hyperpolarized media.

Methods: Recently, we introduced a fast (6 min) and cost-effective method using Spin-Lock Induced Crossing and Signal Amplification By Reversible Exchange (SLIC-SABRE) at µT fields and a rapid purification to produce biocompatible HP solutions of aqueous pyruvate. In this study, we used SLIC-SABRE to conduct in vivo tumor metabolic imaging in a transgenic breast cancer mouse model (MMTV-PyMT).

Results: In agreement with previous HP MRI cancer studies, an elevated lactate metabolism was found in tumors compared to healthy breast tissue, heart, and vasculature, as well as distinct metabolic profiles within different tumor compartments. These findings suggest a potential link between lactate-to-pyruvate ratios and the varying levels of tumor cell proliferation and apoptosis observed by histological analyses.

Conclusion: Our results underscore the potential of SABRE to enhance the accessibility and throughput of HP MRI, thereby advancing cancer research and diagnostic oncology.

Keywords: parahydrogen; hyperpolarization; SABRE; metabolic imaging; MMTV-PyMT

Graphical Abstract:

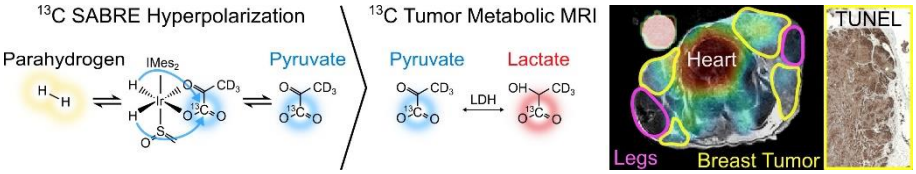

Manuscript short abstract:

Hyperpolarized [1-^{13}C]pyruvate MRI is promising for diagnostic oncology. We demonstrate the high-throughput, user-friendly parahydrogen-based SABRE technology for in-vivo metabolic imaging in breast cancer mice, revealing elevated lactate metabolism and tumor heterogeneity.

Introduction

Cancer remains a significant challenge in modern medicine, with breast cancer representing one of the most prevalent and heterogeneous malignancies [1]. Despite incremental advancements in therapies, including surgery, radiation, and targeted therapies, there remains an urgent medical need to improve clinical outcomes. The complexity of cancer, underscored by its molecular diversity and intratumoral heterogeneity, necessitates personalized approaches for accurate diagnosis and effective treatment guided by non-invasive in vivo imaging [2].

Imaging technologies are playing a pivotal role in cancer care by providing non-invasive assessments of tumor characteristics and treatment responses. Traditional anatomical imaging techniques often cannot provide molecular-level information on cancer development. To address this limitation, molecular imaging techniques have emerged with breakthrough applications [3,4].

Hyperpolarized magnetic resonance imaging (HP MRI) allows for transient signal enhancements of over 10,000-fold [5]. HP MRI offers non-invasive insights into biochemical pathways in vivo without ionizing radiation. HP MRI is the only technology that enables the visualization of metabolic conversion in vivo with spatial and real-time temporal resolution. HP [1-^{13}C]-pyruvate showed great promise for investigating cancer as it is a central metabolite in energy metabolic pathways at the intersection of glycolysis and the TCA cycle. Pyruvate has been used to image metabolism in many cancers, including prostate cancer [6], glioblastoma [7], and bone and liver metastases [8], providing unprecedented insights into tumor biology. Clinically, detecting the Warburg effect - enhanced glycolysis and lactate formation even in the presence of high oxygen levels in tumors - provides essential information regarding tumor grading [9] and active surveillance of therapy response in oncological patients [10–12]. Lactate, the lactate-to-pyruvate ratio and the k_{PL} value were identified as promising biomarkers for tumor aggressiveness, grading and therapy response [9,13–15]. HP [1-^{13}C]-pyruvate MRI is under investigation in over 50 clinical trials [4].

The implementation of HP ^{13}C MRI is currently impeded by several challenges, hindering its widespread application and clinical translation. Notably, these include the short lifetime of the hyperpolarized agent, high cost, the large size of the equipment, low throughput, and the requirement for highly trained personnel, all of which contribute to its slow development.

Dissolution Dynamic Nuclear Polarization (dDNP) is the leading technology for producing HP [1-^{13}C]-pyruvate [16]. It requires strong magnetic fields (typically 5-7 T), cryogenic temperatures (<2 K), and microwave irradiation to polarize agents in the solid phase, followed by rapid thawing and dissolution with superheated water to transfer HP metabolites into the

liquid phase. Preparing HP boluses is elaborate and time-consuming, taking about an hour for a bolus of HP [1-^{13}C]pyruvate; however, many molecular probes can be polarized with dDNP [12,17]. Impressive results of HP MRI have driven ongoing efforts to improve dDNP [18–21] and develop alternative technologies for faster, more versatile, and cost-effective HP media production [22,23].

Parahydrogen-induced polarization (PHIP) [24,25] technologies offer a solution to several challenges by providing rapid hyperpolarization with simple, low-footprint hardware and reduced production costs [22]. PHIP involves the permanent addition of parahydrogen to the substrate through direct or side-arm hydrogenation (PHIP-SAH) [26]. This method, particularly with HP [1-^{13}C]pyruvate, has been used in in vivo cardiac [27] and tumor studies [28–30] in mice and is being developed for commercial preclinical and clinical devices. However, identifying and synthesizing suitable unsaturated precursors is often challenging and costly. Additionally, the chemical modification (i.e., hydrogenation) done seconds before the in vivo administration introduces regulatory complexities and may require manufacturing licenses for clinical applicants in some countries [22].

A non-hydrogenative PHIP referred to as SABRE (Signal Amplification By Reversible Exchange) has been presented by Duckett and coworkers [23,31,32]. SABRE employs a reversible exchange of parahydrogen and suitable substrates with an iridium catalyst [33], allowing for continuous polarization transfer without altering the chemical structure of the substrate [34,35]. Therefore, the method combines the advantages of PHIP - such as speed, low cost, and simplicity - with some of the flexibility of dDNP, which has enabled the ^{13}C and ^{15}N SABRE hyperpolarization of multiple agents [23,36–38], including [1-^{13}C]-pyruvate [32,39–42]. Consequently, the translation of SABRE to preclinical studies and clinical settings is highly promising. Recently, SABRE-SHEATH with a fluorinated catalyst and [1-^{13}C]pyruvate-h_3 was used to perform the first ^{13}C-MR spectroscopy of mice with pancreatic cancer xenografts [43]. We have introduced a fast and cost-effective method using SABRE and Spin-Lock Induced Crossing (SLIC-SABRE) [44,45] at microtesla fields [46,47], which can polarize [1-^{13}C]pyruvate-d_3 to over 20% in methanol-d_4, sufficient for ^{13}C MRI. Initially, this was achieved in a toxic methanol solution containing the iridium-based exchange catalyst. However, a rapid purification process has enabled us to produce HP solutions of aqueous pyruvate suitable for in vivo applications, **Figure 1** [48]. The deuteration of pyruvate results in an increased polarization lifetime without affecting the kinetics of pyruvate metabolism [46,49].

In the present study, we demonstrate ^{13}C MRI of cancer using aqueous [1-^{13}C]pyruvate-d_3 hyperpolarized using SLIC-SABRE. Focusing on transgenic breast cancer mice, we reveal

considerable lactate production and pronounced intra- and intertumoral heterogeneity of the lactate metabolism, which correlates well with histological results.

Methods

50 mM [1-^{13}C]-pyruvate-d_3 was hyperpolarized to up to 24% in 600 µL methanol-d_4 using SLIC-SABRE at a 50 µT static magnetic field. Subsequently, 600 µL phosphate-buffered solution (PBS) of D_2O was added and the sample was evacuated to evaporate methanol-d_4 at approximately 100 mT, 5 mbar, and 100 °C (250 µM residual methanol). The aqueous solution was then filtered to remove the precipitated iridium catalyst, resulting in [1-^{13}C]-pyruvate-d_3 in D_2O solution of pH 6.5 – 7, ready for administration to the mice, **Figure 1**. This way, we efficiently produced a batch of 30 mM aqueous, pH-neutral HP [1-^{13}C]-pyruvate-d_3, hyperpolarized up to $P_{13C} \approx 10\%$ in less than 6 minutes, **Figure S1**.

To investigate the efficacy of SABRE hyperpolarized pyruvate in assessing tumor-specific metabolic processes in vivo, a transgenic breast cancer model (mouse mammary tumor virus – polyomavirus middle tumor-antigen; MMTV-PyMT) was employed [15,50,51]. This viral oncogene activates various oncogenic signals in the mammary epithelium. Most notably, it hyper-activates the phosphoinositide 3-kinase (PI3K) pathway, mimicking a common characteristic observed in approximately 70% of breast cancer patients. The onset of mammary adenomas in MMTV-PyMT mice typically occurs at about 6 weeks of age, rapidly progressing to large, invasive, and poorly differentiated carcinomas within 8 weeks. The numbering of breast tumors and mammary glands is shown in **Figure S2**.

Ethical approval for the animal experiments was obtained from the relevant authority (Regierungspraesidium Freiburg, Talstr. 4-8, 79095 Freiburg; AZ: 35-9185.81/G-21/134). Vital parameters of the rodents were continuously monitored throughout the MRI procedure (see Supporting Information (SI) for details). A cohort of six MMTV-PyMT mice (age: 10-14 weeks, weight: approximately 24 g) exhibiting various tumor stages were investigated.

For MRI, a dedicated mouse ^{1}H/^{13}C quadrature resonator (inner diameter of 3.5 cm, V-XQ-HQ-070-02222, Rapid Biomedical GmbH, Germany) and a 7 T preclinical MRI system (Biospec 70/20, PV6.0.1, Bruker, Germany) were utilized. Following the injection of a single bolus of a 30mM HP [1-^{13}C]-pyruvate-d_3 solution through the tail vein (≤5 µL/g mouse weight), ^{13}C images were acquired using center-out phase encoded free-induction decay chemical shift imaging (FID-CSI) to monitor pyruvate-to-lactate conversion. The FID-CSI sequence was chosen for its known robustness, despite limitations like a broad point spread function (PSF) at small matrix sizes and inefficient use of the hyperpolarized state due to per-phase encode

excitation. This study is the first to use SLIC SABRE for detecting tumor heterogeneity, valuing localized spectroscopic imaging to assess local metabolism without introducing uncertainties from sequence design or complex data analysis. Region-of-interest-based metabolite time curves showed varied profiles, indicating the broad PSF has minimal impact. For data processing, pyruvate and lactate images were generated by time-domain fitting of Free Induction Decay (FID) signals for multiple metabolites (pyruvate, lactate, alanine, pyruvate hydrate) using Python 3.10, minimizing the sum-of-squares difference between measured and modeled data (see supplementary **Figure S3**). For dynamic CSI, images were generated by averaging fitted FID amplitudes across repetitions and then showing the absolute values of the metabolite amplitudes, while single-repetition acquisitions used the absolute amplitudes directly. ROI spectra were computed as weighted averages of magnitude spectra based on voxel coverage within the ROI (see supplementary **Figure S4**). Averaging was done by averaging the absolute spectra across the ROI to avoid signal cancellation due to phase differences. Further experimental details and non-interpolated ^{13}C images (see supplementary **Figure S13**) are provided in the SI.

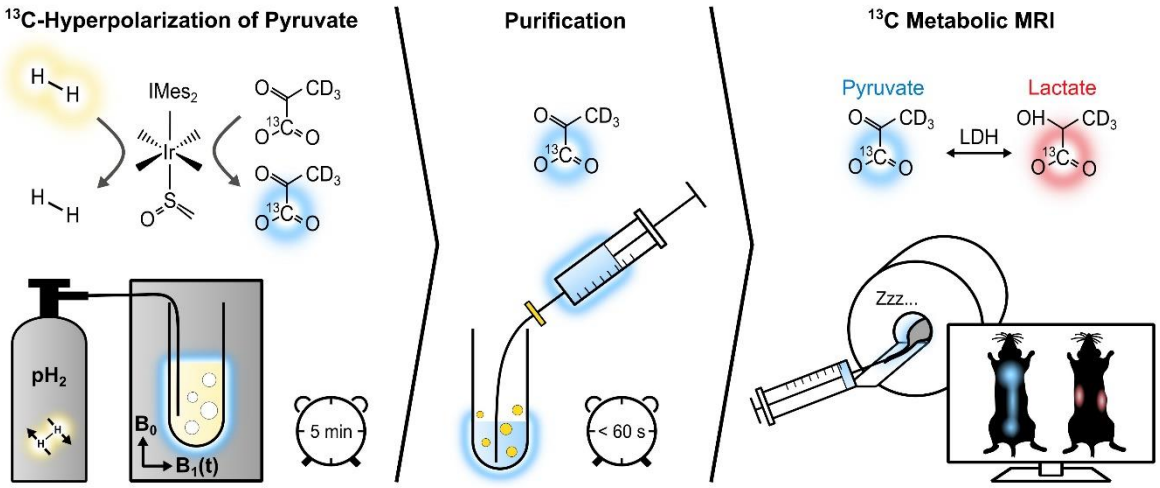

Figure 1. The experimental protocol for in vivo metabolic MRI. Initially, [1-^{13}C]-pyruvate-d_3 undergoes hyperpolarization via reversible exchange with parahydrogen at an iridium complex. Parahydrogen is bubbled through an NMR tube containing the SABRE reaction solution while applying a 2 µT SLIC radiofrequency field in a 50 µT static magnetic field (left). Subsequently, the hyperpolarized [1-^{13}C]-pyruvate-d_3 is transferred from methanol-d_4 to a PBS of D_2O, and the resulting solution is collected in a syringe after filtration to remove the non-water-soluble iridium complex (center). This biocompatible [1-^{13}C]-pyruvate-d_3 solution is then administered to the tumor-bearing mice, allowing for the monitoring of its conversion into downstream metabolic products, i.e., [1-^{13}C]-lactate-d_3 (right).

Results and Discussion

Metabolic imaging revealed prominent lactate metabolism within tumor regions, showcasing the heterogeneous nature of the cancers both anatomically and metabolically. Metabolic imaging results from three of these mice are presented in subsequent sections, while the remaining investigations, along with metabolite signal evolution from all experiments, are provided in the SI.

Mouse A – Localized Metabolic Imaging

Mouse A (age: 13 weeks, weight 24 g) with localized nodules characterized by palpable tumors in all 10 mammary glands. For MRI analysis, an axial region of interest (ROI) was selected that included mammary glands 1, 2, and 7, the lungs, the lower heart ventricles, and the forelimbs, **Figure 2**.

Anatomical ^{1}H MRI revealed distinct tumorous nodes with varying sizes surrounding the forelimbs. The largest observed diameter of a single mammary carcinoma was ≈ 13 mm at gland 1. Most tumor areas exhibited similar T_2w intensity despite differences in node size, **Figure 2**. Intense lactate signals were observed in the tumors. Although the native ^{13}C MRI resolution is limited, the muscles, particularly the front legs, were still distinguishable from the surrounding tumor tissue in the ^{13}C-lactate images, **Figure 2**. Large pyruvate and lactate signals were also observed in the heart, but the lactate-to-pyruvate ratio is negligible compared to the other regions. Analysis of the signal-time curves detected the arrival of the pyruvate bolus and subsequent formation of downstream lactate in the tumor and, to a lesser extent, in the heart, **Figure S5**. Interestingly, when comparing the tumors, the tumor on gland 1 exhibits higher lactate levels and lactate-to-pyruvate ratios compared to the tumors on glands 2 and 7. This observation aligns with the corresponding histology, where Ki67 staining indicates higher cell proliferation levels in tumor 1. In contrast, tumor 7 shows slightly elevated apoptosis and reduced proliferation (see supplementary **Figures S5** and **S15**), which may explain the reduced pyruvate-to-lactate conversion, as reflected by the lower kPL value and lactate-to-pyruvate ratio (see supplementary **Figure S12** and **Table S1**). Note that the high lactate-to-pyruvate (Lac/Pyr) ratio observed in the legs can be attributed, at least in part, to the low pyruvate signal, which is close to the noise level, making the calculated ratio less reliable in these regions. Additionally, due to the 5-mm slice thickness used for the ^{13}C MRI, tumors 1 and 7 partially extend into the area labeled as 'leg' in the displayed 1H MRI. This overlap is not apparent in the 1H MRI, which was acquired with thinner slices (see supplementary **Figure S5G**). The metabolic contributions

of these tumors, combined with partial volume effects, likely account for the elevated ^{13}C Lac/Pyr ratio observed in the leg regions near the tumors.

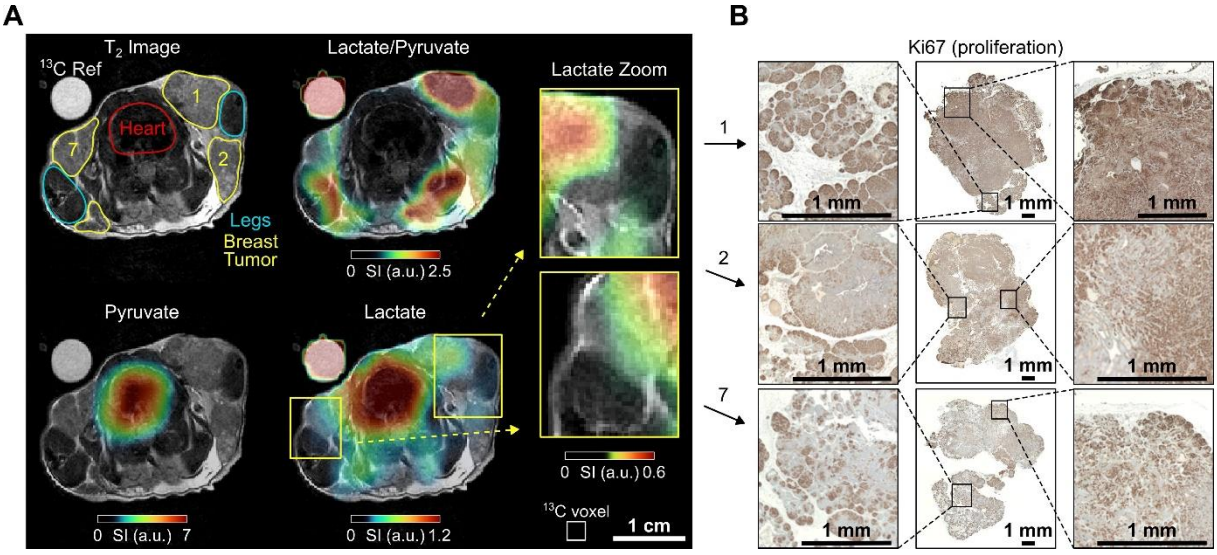

Figure 2. In vivo ^{1}H T_2w MRI and dynamic ^{13}C chemical shift imaging of PyMT mouse A after administering SABRE-hyperpolarized [1-^{13}C]-pyruvate-d_3, and histology (Ki67 staining) of the imaged tumors. (**A)** Axial anatomic ^{1}H MRI showing the tumors on mammary glands 1, 2 and 7, heart, legs, and a ^{13}C-lactate reference (left). The anatomic slice is superimposed with time-summated and interpolated ^{13}C-lactate/^{13}C-pyruvate (top right), ^{13}C-pyruvate (bottom left) and ^{13}C-lactate signal (bottom right). The lactate signal is enhanced in the breast tumors compared to other non-cancerous tissue (e.g., leg muscle). Note that low lactate signals can lead to high lactate-to-pyruvate ratios without significance if the pyruvate signal in the same voxel is negligible (no thresholding was applied to the ratio maps). The apparently elevated 13C signals in the leg and decreased lactate signal in gland 2 can be attributed to partial volume effects and slice positioning, as detailed in Figure S5. The regions indicated as leg and tumor do not exclusively correspond to these anatomical structures within the entire ^{13}C imaging slice. The white box (bottom left) indicates the native CSI-FID resolution. (**B)** Histology of all three breast tumors with Ki67 staining indicates cell proliferation (brown). Remarkably, the tumor on mammary gland 1 has a significantly higher lactate-to-pyruvate ratio and appears to be more proliferative than other tumors**.**

Mouse B – Imaging tumor heterogeneity

Mouse B (age: 12 weeks, weight 24 g) presented with advanced breast cancer characterized by palpable smaller tumors in mammary glands 4 and 9, and larger nodes in glands 2 and 3. No tumor was palpable in the contralateral mammary gland 7. Hence, a cross-section of the upper

chest covering mammary glands 2, 3, and 7 was subjected to MRI analysis to examine differences in tumorous and healthy-appearing breast tissue, **Figure 3**.

Anatomical ^{1}H MRI revealed the tumorous nodes 2 and 3, with approximate maximum diameters of ≈10-12 mm, respectively. Interestingly, while 2 and 3 were similar in size, 3 exhibited a conspicuous tumor area with enhanced intensity in the T_2-weighted MRI images (hyper-intense, T_2w+). Anatomical MRI revealed no apparent abnormalities in gland 7, which additionally appeared significantly smaller compared to 2 and 3, **Figure 3**.

The HP ^{13}C MRI data showed the strongest ^{13}C pyruvate and lactate signals in the heart. The lactate level was elevated in the tumor compared to the contralateral non-cancerous appearing breast tissue (gland 7). The lactate-to-pyruvate ratio map provides additional evidence that the tumor is the primary source of the lactate signal, as the high ratio is most pronounced within the tumor region and at the interface between the tumor and the heart. The T_2w+ region exhibited lower pyruvate and lactate signals than the hypo-intense (T_2w-) region, suggesting lower metabolic activity and perfusion, **Figure 3**. It should be noted that this data was recorded statically at a single time point that started 10 seconds post-injection. At this time, metabolic conversion of pyruvate to lactate was not much advanced, resulting in overall low lactate signals throughout the body compared to the other experiments reported.

The possible correlation between T_2w+ and T_2w- regions and histology is particularly evident in this mouse, **Figure 3B**. The T_2w- area of tumor B exhibits a high proportion (~13%) of necrotic or apoptotic cells, as determined by TUNEL staining, compared to the T_2w+ region, which shows less than 1% cell death (see supplementary **Figure S15**). In contrast, markers of proliferation (Ki67 staining) and vascularization (CD31 staining, see supplementary **Figure S14**) appear unchanged between T_2w hypo- and hyperintense regions. Notably, the Lac/Pyr ratio and overall ^{13}C signal were significantly reduced in the T_2w- area, suggesting a potential association with a higher proportion of non-viable cells.

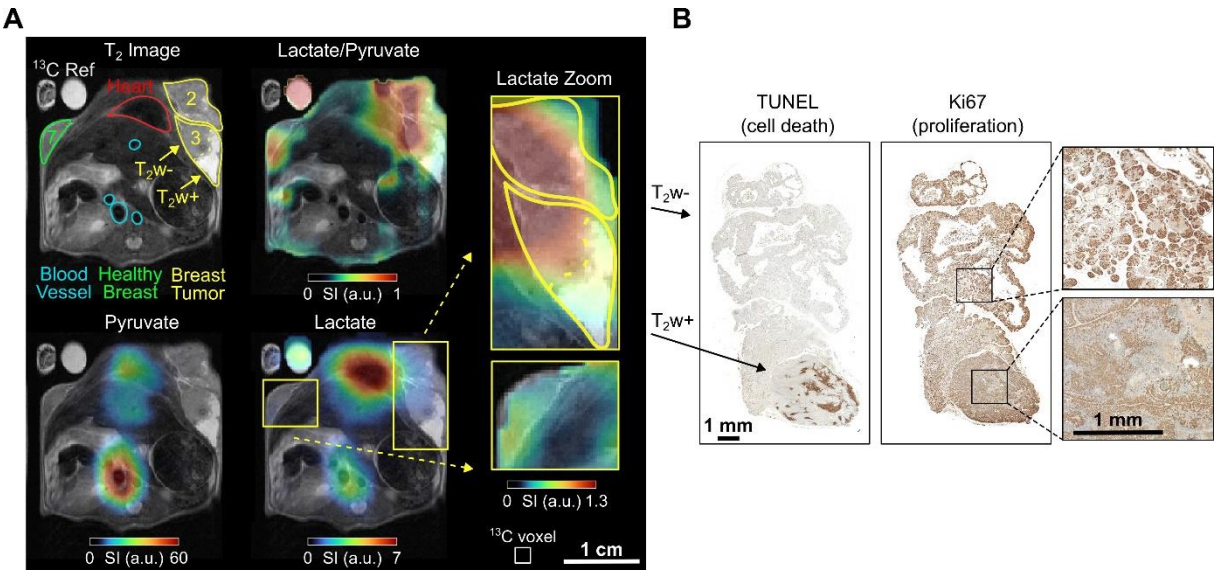

Figure 3. In vivo ^{1}H T_2w MRI and ^{13}C chemical shift imaging of PyMT mouse B after administering SABRE-hyperpolarized [1-^{13}C]-pyruvate-d_3 and histology (Ki67 staining) of the imaged tumors. (**A)** Axial anatomic ^{1}H MRI showing the tumors on mammary glands 2 and 3, non-cancerous appearing breast tissue on gland 7, heart, blood vessels, and a ^{13}C-lactate reference (left). The anatomic slice is superimposed with the interpolated ^{13}C-lactate/^{13}C-pyruvate (top right), ^{13}C-pyruvate (bottom left) and ^{13}C-lactate signal (bottom right). The lactate signal is enhanced in the breast tumors (2 and 3) compared to the non-cancerous appearing breast tissue on mammary gland 7. The heterogeneous breast tumor on mammary gland 3 divides into a hyper-intense (T_2w+) region with lower lactate and lactate-to-pyruvate signals and a hypo-intense (T_2w-) tumor region with higher signals. The pyruvate signal was received from all voxels in the reported regions of interest, see Fig. S6, but is less visible here because of the color scale windowing applied in presence of the strong metabolite signals in the heart and main vessels. Note that histology suggested that the tumors were well vascularized and perfused (see SI Fig. S14). The white box indicates the native CSI-FID resolution. (**B)** Histology of the breast tumor with TUNEL staining indicating ongoing apoptosis in the T_2w+ region (left) and Ki67 staining indicating cell proliferation in the T_2w- region (right).

Mouse C - Imaging tumor heterogeneity

Mouse C (age: 13 weeks, weight 26.7 g) also presented with tumors at mammary glands 1-3, and smaller tumors at 6 and 7. Again, we examined an ROI in the upper body, but the imaging slice was higher positioned compared to the previous experiments, excluding the heart but including a portion of the mouse brain.

Anatomical ^{1}H MRI delineated the tumorous regions, revealing that the tumor in mammary gland 2 had progressed significantly, with a maximum diameter of 13 mm and notable T_2w+

areas, **Figure 4**. This facilitated comparison with previous observations from mouse B, **Figure 3**. In the HP ^{13}C MRI scan, consistent with previous results, robust pyruvate and lactate signals were detected in the tumors. Interestingly, the T_2w+ region again exhibited lower metabolic activity than the surrounding tumor tissue, **Figure 4**. Histological analysis indicated apoptosis onset in the latter region. Note that the elevated lactate-to-pyruvate ratio in the lower right region probably corresponds to an extension of tumor 2. This area additionally shows a low SNR, particularly for the pyruvate signal (see supplementary **Figure S7G**).

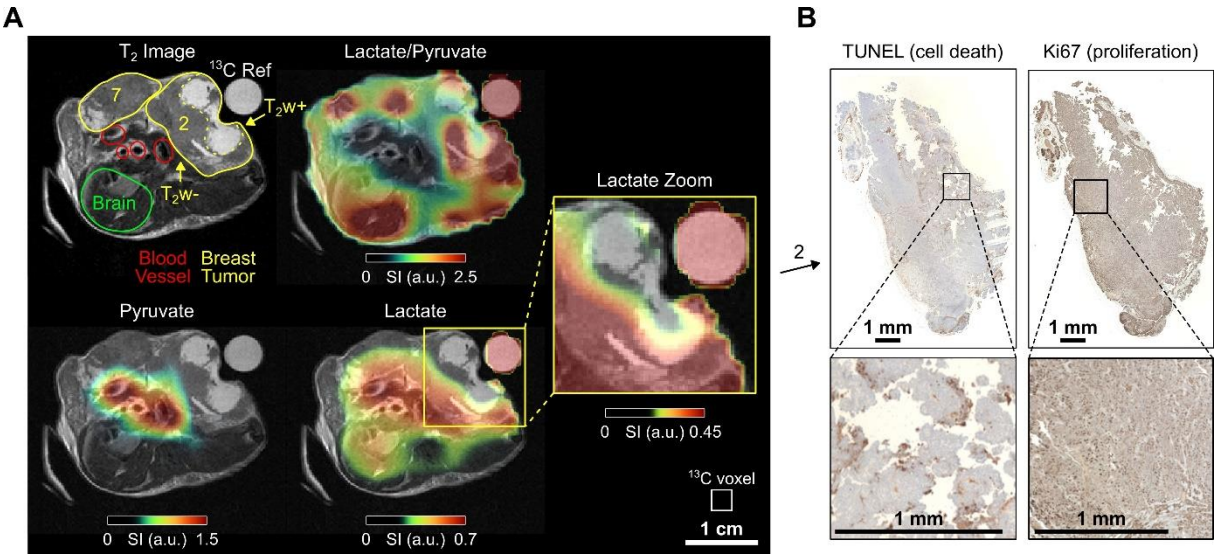

Figure 4. In vivo ^1H T_2w MRI and dynamic ^{13}C chemical shift imaging of PyMT mouse C after administering SABRE-hyperpolarized [1-^{13}C]-pyruvate-d_3 and histology of the imaged tumor. (**A)** Axial anatomic ^1H MRI showing the tumors on mammary glands 2 and 7, brain, blood vessels, and a ^{13}C-lactate reference (left). The anatomic slice is superimposed with time-summated and interpolated ^{13}C-lactate/^{13}C-pyruvate (top right), ^{13}C-pyruvate (bottom left) and ^{13}C-lactate signal (bottom right). The heterogeneous breast tumor in mammary gland 2 divides into a hyper-intense (T_2w+) region with lower lactate and lactate-to-pyruvate signals and a hypo-intense (T_2w-) tumor region with higher signal. Note that low lactate signals can lead to high lactate-to-pyruvate ratios without significance if the pyruvate signal in the same voxel is negligible (no thresholding was applied to the ratio maps). The white box indicates the native CSI-FID resolution. (**B)** Histology of the hypointense tumor region with TUNEL staining indicating ongoing apoptosis (left) and Ki67 staining indicating cell proliferation (right).

Summary of other mice and comparison

Three additional mice, D, E, and F, aged 12, 14, and 14 weeks respectively, were examined as detailed in the supplementary information (SI). They also exhibited localized tumor formations, consistent with observations from previous experiments, characterized by elevated ^{13}C signals and lactate metabolism in tumor areas compared to healthy tissue, e.g., **Figure S9 and S10**. As previously described, T_2w+ and necrotic regions showed meager ^{13}C signals, i.e. were metabolically less active, **Figure S8**. In some cases, the tumors exhibited poor pyruvate signals but strong lactate signals, indicating rapidly metabolized pyruvate (mice B and C, **Figure S8)**. The lactate-to-pyruvate ratios of different regions (T_2w+, T_2w-, and heart/blood vessel) from all six mice are compared in **Figure 5A**. T_2w- tumor regions exhibit a higher lactate-to-pyruvate ratio compared to T_2w+ tumor or heart/blood vessel regions, with a significant difference observed between T_2w- and heart/blood vessel tissues (p = 0.0052). Pyruvate-to-lactate rate constants k_{PL} were derived from a kinetic model fitted to the dynamic data. A comparison of k_{PL} in T_2w- tumor and heart/blood vessel regions is presented in **Figure 5B**, revealing a significant difference (p = 0.0060). The weighted averages of the k_{PL} in those regions are $k_{PL,T2w-}$ = 0.081(13) 1/s, $k_{PL,Heart/Vessel}$ = 0.0234(17) 1/s. Notably, a previous publication investigated the same breast cancer mouse model and supports the k_{PL} elevation compared to healthy tissue [15,52]. Both trends, higher lactate-to-pyruvate ratios and elevated k_{PL} values in T_2w- tumor regions, were observed across all mice, as shown in **Figures S11 and S12**.

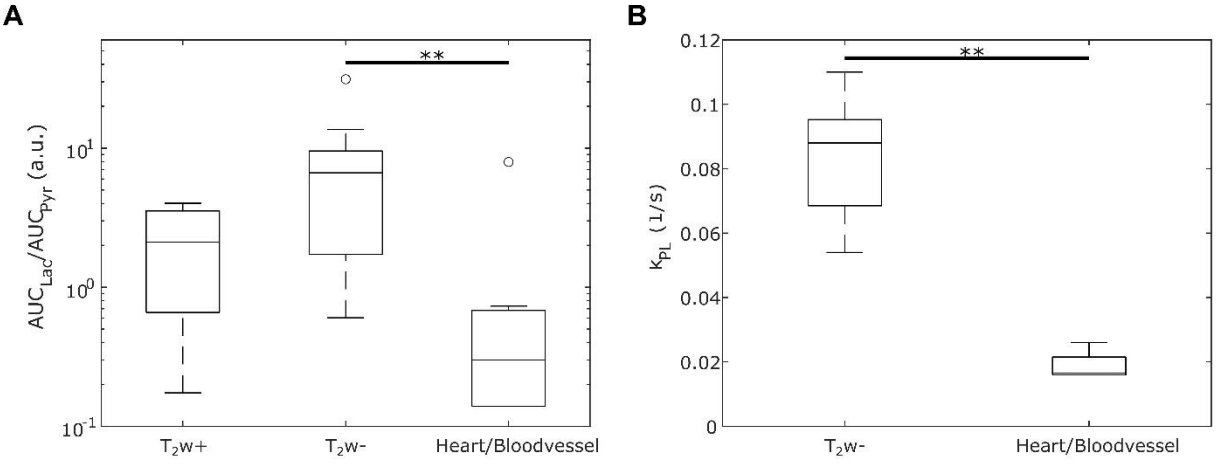

Figure 5. Box-and-whiskers plot depicting **(A)** the spectral lactate-to-pyruvate ratios and **(B)** the kinetic lactate-to-pyruvate rate constant k_{PL} across different regions in six mice: Hyperintense tumor (T_2w+), hypointense tumor (T_2w-), and heart resp. blood vessel (depending on the mouse). The significant difference between the T_2w- and heart/blood vessel regions is marked with ** (p < 0.01).

Significance and Conclusion

Breast cancer is one of the most prevalent tumor entities and has been studied extensively with dDNP-based HP MRI [53,54]. Also, the MMTV-PyMT mouse model has been studied before [15]. In this pilot study, we applied the less complex, low-cost, high-throughput SABRE approach for the first time to tumor imaging. Our methodology enables rapid preparation of HP pyruvate without chemical modification for in vivo use within six minutes, utilizing a cost-effective (<10,000 €), self-constructed setup.

In agreement with previous studies, we found elevated lactate formation as a manifestation of the Warburg effect in the tumors. Notably, we identified regional differences in pyruvate metabolism within the tumors in the ^{13}C MRI. These findings correlated with histological results, particularly with cell proliferation and apoptosis staining.

We utilized transgenic MMTV-PyMT breast cancer mice [15,50,51]. Tumor growth was fast, and substantial variations were observed between the six mice investigated. Via histology, we observed cell death onset within some tumors as the animals approached the ethical study endpoint regarding the primary tumor burden. Although this diversity in tumor stages complicates potential studies, the model is particularly intriguing because the mice hyper-activate key molecular pathways associated with breast cancer, such as PI3K signaling. The resulting stepwise tumor progression mirrors the tumor histopathology as well as the tumor stages of breast cancer patients. Therefore, the primary tumors of the MMTV-PyMT model present a range of metabolic tumor phenotypes that are likely to be encountered in clinical imaging studies. Notably, the clinical value of HP MRI has already been demonstrated in multiple clinical studies, including improved grading [9] and risk stratification for prostate cancer patients and characterization of tumor heterogeneity in glioblastoma [55]. Recent reports showed the capability of HP MRI to monitor treatment response to neoadjuvant chemotherapy in breast cancer patients within days [11]. Thus, the development of faster, cost-effective technologies is crucial for increasing the availability of this promising molecular imaging technique.

SABRE aims to address these issues. However, while the polarization levels currently achieved with SLIC-SABRE are sufficient for preclinical studies, they remain lower than those typically obtained with dDNP. This discrepancy limits its immediate applicability in settings requiring ultra-high signal-to-noise ratios. Similarly, PHIP has made significant advancements in recent years, achieving polarization levels comparable to dDNP. Yet, SABRE offers unique advantages, including a broader range of hyperpolarizable molecules and the absence of a chemical reaction shortly before injection. A key challenge for SABRE, however, are the short

T_1 relaxation times of some substrates during polarization build-up, which constrains the achievable polarization levels. It is worth mentioning that both dDNP and PHIP polarizers are already commercially available for preclinical applications.

Despite its advantages, translating SABRE to clinical applications will require significant effort, such as upscaling and enhanced purification of the contrast agent solutions. While our method, i.e. catalyst precipitation and methanol evaporation, currently reduces toxicity to acceptable levels in preclinical studies, further development of automated and scalable purification protocols is needed to ensure clinical safety. The currently remaining quantities of methanol and iridium are about one order of magnitude higher than permitted for clinical injection solutions.

While this pilot study provides a valuable demonstration, further research is required to build on these findings. Additional control studies are envisioned - such as imaging younger mice before apoptosis onset, longitudinal animal monitoring, and incorporating direct perfusion measurements - to provide deeper insights into the progression of tumors and the evolution of metabolic alterations, particularly the lactate-to-pyruvate ratio. These insights may help define biomarker thresholds indicative of tumor onset.

In conclusion, the present study demonstrates, for the first time, metabolic imaging of tumors with SLIC-SABRE hyperpolarized pyruvate. We have demonstrated that SABRE delivers the signal enhancement needed for detecting metabolic spatial differences in complex tumor tissue, possibly linked to different grades of proliferation and apoptosis. Note that with improved sequences, we also expect enhanced SNR and higher-quality images [56,57]. To improve spatial accuracy and coregistration of regions of interest and mitigate partial volume effects, super-resolution techniques, such as patch-based reconstruction or volumetric super-resolution, may offer a viable approach to effectively reduce the thickness of the ^{13}C slice [58]. This study demonstrates that SABRE has matured enough to allow cancer studies, significantly enhancing access to HP as a powerful molecular imaging tool and being a promising candidate for clinical translation.

Abbreviations

HP: hyperpolarization/hyperpolarized; MRI: magnetic resonance imaging; TCA: tricarboxylic acid; dDNP: dissolution dynamic nuclear polarization; PHIP: parahydrogen-induced polarization; PHIP-SAH: parahydrogen-induced polarization side-arm hydrogenation; SABRE: signal amplification by reversible exchange; SLIC-SABRE: spin-lock induced crossing signal amplification by reversible exchange; PBS: phosphate-buffered solution; MMTV-PyMT: mouse mammary tumor virus – polyomavirus middle tumor-antigen; PI3K: phosphoinositide 3-kinase; FID-CSI: free-induction decay chemical shift imaging; ROI: region of interest; T_2w+: T_2 hyper-intense; T_2w-: T_2 hypo-intense; TUNEL: terminal deoxynucleotidyl transferase dUTP nick end labeling

Supporting Information

Please find additional experimental details, MRI, and mice data in the Supporting Information file. The authors have cited additional references within the SI [59–63].

Acknowledgments

Research reported in this publication was supported by the German Federal Ministry of Education and Research (BMBF) in the funding program "Quantum Technologies – from Basic Research to Market" under the project "QuE-MRT" (contract number: 13N16448, 13N16450), the German Cancer Consortium (DKTK), the DKTK joint funding HYPERBOLIC, the Research Commission of the University Medical Center Freiburg, the Core Facility AMIR^{CF} (DFG-RIsources N° RI_00052, INST 39/1224-1), B.E.S.T. Fluidsysteme GmbH I Swagelok Stuttgart, and the German Research Foundation (DFG #SCHM 3694/1-1, #SCHM 3694/2-1, #SFB1479, #HO4604/4-1, #HO4604/5-1, #FOR5042, #GRK2606/423813989), BMBF BlueHealthTech 03WIR6208A. This work was supported by the Cluster of Excellence iFIT (EXC 2180) "Image-Guided and Functionally Instructed Tumor Therapies", University of Tuebingen, Germany. EYC thanks NIBIB R21 EB033872. We acknowledge support by the Open Access Publication Fund of the University of Freiburg.

Conflicts of Interest

SK and IS are with NVision Imaging Technologies GmbH. FS serves on the scientific advisory board of NVision Imaging Technologies GmbH. EYC holds a stake of ownership in XeUS Technologies Ltd. and serves on the scientific advisory board of Vizma Life Sciences LLC. The other authors have no competing interests to declare.

References

1. Zardavas D, Irrthum A, Swanton C, Piccart M. Clinical management of breast cancer heterogeneity. Nat Rev Clin Oncol. 2015; 12: 381–94.

2. Rowe SP, Pomper MG. Molecular imaging in oncology: Current impact and future directions. CA Cancer J Clin. 2022; 72: 333–52.

3. Wang ZJ, Ohliger MA, Larson PE, Gordon JW, Bok RA, Slater J, et al. Hyperpolarized 13C MRI: state of the art and future directions. Radiology. 2019; 291: 273.

4. Chaumeil MM, Bankson JA, Brindle KM, Epstein S, Gallagher FA, Grashei M, et al. New Horizons in Hyperpolarized 13C MRI. Mol Imaging Biol [Internet]. 2023 [cited 28 December 2023]; Available at: https://doi.org/10.1007/s11307-023-01888-5

5. Ardenkjær-Larsen JH, Fridlund B, Gram A, Hansson G, Hansson L, Lerche MH, et al. Increase in signal-to-noise ratio of > 10,000 times in liquid-state NMR. Proc Natl Acad Sci. 2003; 100: 10158–63.

6. Kurhanewicz J, Vigneron DB, Ardenkjaer-Larsen JH, Bankson JA, Brindle K, Cunningham CH, et al. Hyperpolarized 13C MRI: Path to Clinical Translation in Oncology. Neoplasia. 2019; 21: 1–16.

7. Zaccagna F, McLean MA, Grist JT, Kaggie J, Mair R, Riemer F, et al. Imaging Glioblastoma Metabolism by Using Hyperpolarized [1-13C]Pyruvate Demonstrates Heterogeneity in Lactate Labeling: A Proof of Principle Study. Radiol Imaging Cancer. 2022; 4: e210076.

8. Chen H-Y, Aggarwal R, Bok RA, Ohliger MA, Zhu Z, Lee P, et al. Hyperpolarized 13C-pyruvate MRI detects real-time metabolic flux in prostate cancer metastases to bone and liver: a clinical feasibility study. Prostate Cancer Prostatic Dis. 2020; 23: 269–76.

9. Chowdhury R, Mueller CA, Smith L, Gong F, Papoutsaki M-V, Rogers H, et al. Quantification of Prostate Cancer Metabolism Using 3D Multiecho bSSFP and Hyperpolarized [1-13C] Pyruvate: Metabolism Differs Between Tumors of the Same Gleason Grade. J Magn Reson Imaging. 2023; 57: 1865–75.

10. Sushentsev N, McLean MA, Warren AY, Benjamin AJV, Brodie C, Frary A, et al. Hyperpolarised 13C-MRI identifies the emergence of a glycolytic cell population within intermediate-risk human prostate cancer. Nat Commun. 2022; 13: 466.

11. Woitek R, McLean MA, Ursprung S, Rueda OM, Manzano Garcia R, Locke MJ, et al. Hyperpolarized Carbon-13 MRI for Early Response Assessment of Neoadjuvant Chemotherapy in Breast Cancer Patients. Cancer Res. 2021; 81: 6004–17.

12. Woitek R, Brindle KM. Hyperpolarized Carbon-13 MRI in Breast Cancer. Diagnostics. 2023; 13: 2311.

13. Albers MJ, Bok R, Chen AP, Cunningham CH, Zierhut ML, Zhang VY, et al. Hyperpolarized 13C Lactate, Pyruvate, and Alanine: Noninvasive Biomarkers for Prostate Cancer Detection and Grading. Cancer Res. 2008; 68: 8607–15.

14. Ursprung S, Woitek R, McLean MA, Priest AN, Crispin-Ortuzar M, Brodie CR, et al. Hyperpolarized 13C-Pyruvate Metabolism as a Surrogate for Tumor Grade and Poor Outcome in Renal Cell Carcinoma—A Proof of Principle Study. Cancers. 2022; 14: 335.

15. Asghar Butt S, Søgaard LV, Ardenkjaer-Larsen JH, Lauritzen MH, Engelholm LH, Paulson OB, et al. Monitoring mammary tumor progression and effect of tamoxifen treatment in MMTV-PymT using MRI and magnetic resonance spectroscopy with hyperpolarized [1-13C]pyruvate. Magn Reson Med. 2015; 73: 51–8.

16. Ardenkjaer-Larsen JH. On the present and future of dissolution-DNP. J Magn Reson. 2016; 264: 3–12.

17. Park H, Wang Q. State-of-the-art accounts of hyperpolarized 15 N-labeled molecular imaging probes for magnetic resonance spectroscopy and imaging. Chem Sci. 2022; 13: 7378–91.

18. Ardenkjær-Larsen JH, Bowen S, Petersen JR, Rybalko O, Vinding MS, Ullisch M, et al. Cryogen-free dissolution dynamic nuclear polarization polarizer operating at 3.35 T, 6.70 T, and 10.1 T. Magn Reson Med. 2019; 81: 2184–94.

19. Capozzi A, Cheng T, Boero G, Roussel C, Comment A. Thermal annihilation of photo-induced radicals following dynamic nuclear polarization to produce transportable frozen hyperpolarized 13C-substrates. Nat Commun. 2017; 8: 15757.

20. Jannin S, Bornet A, Melzi R, Bodenhausen G. High field dynamic nuclear polarization at 6.7 T: Carbon-13 polarization above 70% within 20 min. Chem Phys Lett. 2012; 549: 99–102.

21. Stern Q, Reynard-Feytis Q, Elliott SJ, Ceillier M, Cala O, Ivanov K, et al. Rapid and Simple 13C-Hyperpolarization by 1H Dissolution Dynamic Nuclear Polarization Followed by an Inline Magnetic Field Inversion. J Am Chem Soc. 2023; 145: 27576–86.

22. Schmidt AB, Bowers CR, Buckenmaier K, Chekmenev EY, de Maissin H, Eills J, et al. Instrumentation for Hydrogenative Parahydrogen-Based Hyperpolarization Techniques. Anal Chem. 2022; 94: 479–502.

23. Salnikov OG, Burueva DB, Skovpin IV, Koptyug IV. Parahydrogen-based NMR signal amplification by reversible exchange (SABRE): Recent advances and applications. Mendeleev Commun. 2023; 33: 583–96.

24. Bowers CR, Weitekamp DP. Parahydrogen and synthesis allow dramatically enhanced nuclear alignment. J Am Chem Soc. 1987; 109: 5541–2.

25. Eisenschmid TC, Kirss RU, Deutsch PP, Hommeltoft SI, Eisenberg R, Bargon J, et al. Para hydrogen induced polarization in hydrogenation reactions. J Am Chem Soc. 1987; 109: 8089–91.

26. Reineri F, Boi T, Aime S. ParaHydrogen Induced Polarization of 13C carboxylate resonance in acetate and pyruvate. Nat Commun. 2015; 6: 5858.

27. Cavallari E, Carrera C, Sorge M, Bonne G, Muchir A, Aime S, et al. The 13C hyperpolarized pyruvate generated by ParaHydrogen detects the response of the heart to altered metabolism in real time. Sci Rep. 2018; 8: 8366.

28. Hune T, Mamone S, Schroeder H, Jagtap AP, Sternkopf S, Stevanato G, et al. Metabolic Tumor Imaging with Rapidly Signal-Enhanced 1-13C-Pyruvate-d3. ChemPhysChem. 2023; 24: e202200615.

29. Fries L, Hune T, Sternkopf S, Mamone S, Schneider KL, Schulz-Heddergott R, et al. Real-Time Metabolic Magnetic Resonance Spectroscopy of Pancreatic and Colon Cancer Tumor-Xenografts with Parahydrogen Hyperpolarized 1-13C Pyruvate-d3. Chem – Eur J. n/a: e202400187.

30. Nagel L, Gierse M, Gottwald W, Ahmadova Z, Grashei M, Wolff P, et al. Parahydrogen-Polarized [1-13C]Pyruvate for Reliable and Fast Preclinical Metabolic Magnetic Resonance Imaging. Adv Sci. 2023; 10: 2303441.

31. Adams RW, Aguilar JA, Atkinson KD, Cowley MJ, Elliott PIP, Duckett SB, et al. Reversible Interactions with para-Hydrogen Enhance NMR Sensitivity by Polarization Transfer. Science. 2009; 323: 1708–11.

32. Iali W, Roy SS, Tickner BJ, Ahwal F, Kennerley AJ, Duckett SB. Hyperpolarising Pyruvate through Signal Amplification by Reversible Exchange (SABRE). Angew Chem Int Ed. 2019; 58: 10271–5.

33. Cowley MJ, Adams RW, Atkinson KD, Cockett MCR, Duckett SB, Green GGR, et al. Iridium N-Heterocyclic Carbene Complexes as Efficient Catalysts for Magnetization Transfer from para-Hydrogen. J Am Chem Soc. 2011; 133: 6134–7.

34. Barskiy DA, Kovtunov KV, Koptyug IV, He P, Groome KA, Best QA, et al. In Situ and Ex Situ Low-Field NMR Spectroscopy and MRI Endowed by SABRE Hyperpolarization. ChemPhysChem. 2014; 15: 4100–7.

35. Hövener J-B, Schwaderlapp N, Lickert T, Duckett SB, Mewis RE, Highton LAR, et al. A hyperpolarized equilibrium for magnetic resonance. Nat Commun. 2013; 4: 2946.

36. Theis T, Truong ML, Coffey AM, Shchepin RV, Waddell KW, Shi F, et al. Microtesla SABRE Enables 10% Nitrogen-15 Nuclear Spin Polarization. J Am Chem Soc. 2015; 137: 1404–7.

37. Zhivonitko VV, Skovpin IV, Koptyug IV. Strong 31P nuclear spin hyperpolarization produced via reversible chemical interaction with parahydrogen. Chem Commun. 2015; 51: 2506–9.

38. Hövener J-B, Pravdivtsev AN, Kidd B, Bowers CR, Glöggler S, Kovtunov KV, et al. Parahydrogen-Based Hyperpolarization for Biomedicine. Angew Chem Int Ed. 2018; 57: 11140–62.

39. Chapman B, Joalland B, Meersman C, Ettedgui J, Swenson RE, Krishna MC, et al. Low-Cost High-Pressure Clinical-Scale 50% Parahydrogen Generator Using Liquid Nitrogen at 77 K. Anal Chem. 2021; 93: 8476–83.

40. Adelabu I, TomHon P, Kabir MSH, Nantogma S, Abdulmojeed M, Mandzhieva I, et al. Order-Unity 13C Nuclear Polarization of [1-13C]Pyruvate in Seconds and the Interplay of Water and SABRE Enhancement. ChemPhysChem. 2022; 23: e202100839.

41. Schmidt AB, de Maissin H, Adelabu I, Nantogma S, Ettedgui J, TomHon P, et al. Catalyst-Free Aqueous Hyperpolarized [1-13C]Pyruvate Obtained by Re-Dissolution Signal Amplification by Reversible Exchange. ACS Sens. 2022; 7: 3430–9.

42. MacCulloch K, Browning A, Guarin Bedoya DO, McBride SJ, Abdulmojeed MB, Dedesma C, et al. Facile hyperpolarization chemistry for molecular imaging and metabolic tracking of [1–13C]pyruvate in vivo. J Magn Reson Open. 2023; 16–17: 100129.

43. Ettedgui J, Yamamoto K, Blackman B, Koyasu N, Raju N, Vasalatiy O, et al. In vivo Metabolic Sensing of Hyperpolarized [1-13C]Pyruvate in Mice Using a Recyclable Perfluorinated Iridium Signal Amplification by Reversible Exchange Catalyst. Angew Chem Int Ed. 2024; 63: e202407349.

44. DeVience SJ, Walsworth RL, Rosen MS. Preparation of Nuclear Spin Singlet States Using Spin-Lock Induced Crossing. Phys Rev Lett. 2013; 111: 173002.

45. Theis T, Truong M, Coffey AM, Chekmenev EY, Warren WS. LIGHT-SABRE enables efficient in-magnet catalytic hyperpolarization. J Magn Reson. 2014; 248: 23–6.

46. Schmidt AB, Eills J, Dagys L, Gierse M, Keim M, Lucas S, et al. Over 20% Carbon-13 Polarization of Perdeuterated Pyruvate Using Reversible Exchange with Parahydrogen and Spin-Lock Induced Crossing at 50 μT. J Phys Chem Lett. 2023; 14: 5305–9.

47. Pravdivtsev AN, Buckenmaier K, Kempf N, Stevanato G, Scheffler K, Engelmann J, et al. LIGHT-SABRE Hyperpolarizes 1-13C-Pyruvate Continuously without Magnetic Field Cycling. J Phys Chem C. 2023; 127: 6744–53.

48. de Maissin H, Groß PR, Mohiuddin O, Weigt M, Nagel L, Herzog M, et al. In Vivo Metabolic Imaging of [1-13C]Pyruvate-d3 Hyperpolarized By Reversible Exchange With Parahydrogen**. Angew Chem Int Ed. 2023; 62: e202306654.

49. Funk AM, Wen X, Hever T, Maptue NR, Khemtong C, Sherry AD, et al. Effects of deuteration on transamination and oxidation of hyperpolarized 13C-Pyruvate in the isolated heart. J Magn Reson. 2019; 301: 102–8.

50. Ketterer S, Mitschke J, Ketscher A, Schlimpert M, Reichardt W, Baeuerle N, et al. Cathepsin D deficiency in mammary epithelium transiently stalls breast cancer by interference with mTORC1 signaling. Nat Commun. 2020; 11: 5133.

51. Attalla S, Taifour T, Bui T, Muller W. Insights from transgenic mouse models of PyMT-induced breast cancer: recapitulating human breast cancer progression in vivo. Oncogene. 2021; 40: 475–91.

52. Larson PEZ, Bernard JML, Bankson JA, Bøgh N, Bok RA, Chen AP, et al. Current methods for hyperpolarized [1-C]pyruvate MRI human studies. Magn Reson Med. 2024; 91: 2204–28.

53. Woitek R, Brindle KM. Hyperpolarized Carbon-13 MRI in Breast Cancer. Diagnostics. 2023; 13: 2311.

54. Arponen O, Wodtke P, Gallagher FA, Woitek R. Hyperpolarised 13C-MRI using 13C-pyruvate in breast cancer: A review. Eur J Radiol. 2023; 167: 111058.

55. Nelson SJ, Kurhanewicz J, Vigneron DB, Larson PEZ, Harzstark AL, Ferrone M, et al. Metabolic Imaging of Patients with Prostate Cancer Using Hyperpolarized [1-13C]Pyruvate. Sci Transl Med. 2013; 5: 198ra108-198ra108.

56. Larson PEZ, Bernard JML, Bankson JA, Bøgh N, Bok RA, Chen AP, et al. Current methods for hyperpolarized [1-13C]pyruvate MRI human studies. Magn Reson Med. 2024; 91: 2204–28.

57. Gordon JW, Chen H-Y, Dwork N, Tang S, Larson PEZ. Fast Imaging for Hyperpolarized MR Metabolic Imaging. J Magn Reson Imaging. 2021; 53: 686–702.

58. Ehrhardt MJ, Gallagher FA, McLean MA, Schönlieb C-B. Enhancing the spatial resolution of hyperpolarized carbon-13 MRI of human brain metabolism using structure guidance. Magn Reson Med. 2022; 87: 1301–12.

59. Savka R, Plenio H. Facile synthesis of [(NHC)MX(cod)] and [(NHC)MCl(CO)2] (M = Rh, Ir; X = Cl, I) complexes. Dalton Trans. 2014; 44: 891–3.

60. Hövener J-B, Bär S, Leupold J, Jenne K, Leibfritz D, Hennig J, et al. A continuous-flow, high-throughput, high-pressure parahydrogen converter for hyperpolarization in a clinical setting. NMR Biomed. 2013; 26: 124–31.

61. Kiryutin AS, Sauer G, Hadjiali S, Yurkovskaya AV, Breitzke H, Buntkowsky G. A highly versatile automatized setup for quantitative measurements of PHIP enhancements. J Magn Reson. 2017; 285: 26–36.

62. Nantogma S, Chowdhury MRH, Kabir MSH, Adelabu I, Joshi SM, Samoilenko A, et al. MATRESHCA: Microtesla Apparatus for Transfer of Resonance Enhancement of Spin Hyperpolarization via Chemical Exchange and Addition. Anal Chem. 2024; 96: 4171–9.

63. Lin EY, Jones JG, Li P, Zhu L, Whitney KD, Muller WJ, et al. Progression to malignancy in the polyoma middle T oncoprotein mouse breast cancer model provides a reliable model for human diseases. Am J Pathol. 2003; 163: 2113–26.